

Discovery of Superconductivity in (Ba,K)SbO₃

Minu Kim¹, Graham M. McNally¹, Hun-Ho Kim¹, Mohamed Oudah², Alexandra Gibbs³, Pascal Manuel³, Robert Green^{2,4}, Tomohiro Takayama¹, Alexander Yaresko¹, Ulrich Wedig¹, Masahiko Isobe¹, Reinhard K. Kremer¹, D. A. Bonn², Bernhard Keimer¹, and Hidenori Takagi^{1,5}

¹Max Planck Institute for Solid State Research, Heisenbergstrasse 1, 70569 Stuttgart, Germany.

²Stewart Blusson Quantum Matter Institute, University of British Columbia, Vancouver, British Columbia V6T 1Z4, Canada.

³ISIS Facility, STFC Rutherford Appleton Laboratory, Harwell Science and Innovation Campus, Oxon OX11 0QX, United Kingdom.

⁴Department of Physics & Engineering Physics, University of Saskatchewan, Saskatoon, Saskatchewan S7N 5E2, Canada.

⁵Department of Physics, University of Tokyo, Bunkyo-ku, Hongo 7-3-1, Tokyo 113-0033, Japan.

Superconducting bismuthates (Ba,K)BiO₃ (BKBO) constitute an interesting class of superconductors in that superconductivity with a remarkably high T_c of 30 K^{1,2} arises in proximity to charge density wave (CDW) order. Prior understanding on the driving mechanism of the CDW and superconductivity emphasizes the role of either bismuth (negative U model)^{3,4} or oxygen ions (ligand hole model)^{5,6}. While holes in BKBO presumably reside on oxygen owing to their negative charge transfer energy, so far there has been no other comparative material studied. Here, we introduce (Ba,K)SbO₃ (BKSO) in which the Sb 5s orbital energy is higher than that of the Bi 6s orbitals enabling tuning of the charge transfer energy from negative to slightly positive. The parent compound BaSbO_{3- δ} shows a larger CDW gap compared to the undoped bismuthate BaBiO₃. As the CDW order is suppressed via potassium substitution up to 65 %, superconductivity emerges, rising up to $T_c = 15$ K. This value is lower than the maximum T_c of BKBO, but higher by more than a factor of two at comparable potassium concentrations. The discovery of an enhanced CDW gap and superconductivity in BKSO indicates that the sign of the charge transfer energy may not be crucial, but instead strong metal-oxygen covalency plays the essential role in constituting a CDW and high- T_c superconductivity in the main-group perovskite oxides.

Superconducting bismuthates, $\text{BaPb}_{1-x}\text{Bi}_x\text{O}_3$ (BPBO)⁷ and $\text{Ba}_{1-x}\text{K}_x\text{BiO}_3$ (BKBO)^{1,2}, have attracted considerable research interest since their discovery more than three decades ago. The parent compound BaBiO_3 (BBO) is known to be a non-magnetic, commensurate charge density wave (CDW) insulator. The CDW order is accompanied by a breathing octahedral distortion, that is, two octahedra with different sizes order in a three-dimensional checkerboard pattern^{8,9}. As the CDW order is suppressed via chemical substitution of Ba with K or Bi with Pb^{10,11}, the compounds become superconducting up to a maximum T_c of 12 K in BPBO, and 30 K in BKBO. Numerous experiments have established that the mechanism of superconductivity is largely conventional; the pairing symmetry is s -wave¹², and the oxygen isotope effect is consistent with the BCS theory¹³, meaning electron-phonon interaction plays the important role in superconductivity. Nevertheless, the unexpectedly high T_c of BKBO, despite a rather low carrier density, has triggered various critical questions as to the driving mechanism and the correct model of the CDW order and superconductivity in these materials. Recent studies suggest that the additional consideration of long-range exchange interactions and many-body effects can be crucial for the quantitative description of the CDW gap^{14,15} as well as for superconductivity¹⁶⁻¹⁸.

Historically, superconducting bismuthates have been considered as archetypal candidates for unconventional superconductors in which an effective attractive electron-electron interaction (negative U ^{19,20}) leads to electron pairing in real as well as in momentum spaces^{3,4}. The real-space pairing occurs in the parent compound BBO, which is argued to be a typical valence-skipping compound with unstable tetravalent bismuth ($6s^1$) disproportionated into tri- ($6s^2$) and pentavalent ($6s^0$). As the charge disproportionation on the bismuth sites is suppressed via chemical doping and the bismuth valence starts to dynamically fluctuate, negative U , which causes pairing of two electrons in the $\text{Bi}^{3+}\text{-O}_6$ octahedra, could also pair them in k -space, leading

to bipolaronic superconductivity. Although its direct evidence still remains to be clarified, the model has provided a possible framework to understand superconductivity in the bismuthates as well as some chalcogenides²¹ with valence-skipping elements.

While the negative U model emphasizes the role of bismuth, an alternative model asserts the role of oxygen and its hybridization with bismuth^{5,6,10,22}. Its foundation is that the charge transfer energy Δ_{CT} of the bismuthates is negative, as the on-site energy of the Bi 6s orbital is lower than that of the oxygen 2p owing to the large relativistic effect of heavy bismuth²³. Consequently, electronic states around the Fermi level (which originate from the strongly hybridized $sp\sigma^*$ antibonding states) show predominantly oxygen 2p character. This crucially modifies the preceding understanding of the CDW order in BBO; it should be described not by the charge disproportionation ($6s^2 + 6s^0$) but rather by the bond-length disproportionation as $6s^2 + 6s^2\bar{L}^2$, where \bar{L} denotes a ligand hole. Spectroscopic evidence supports the oxygen hole model^{24,25}. As the CDW order is suppressed, oxygen holes become delocalized, giving rise to superconductivity, possibly via strong electron-phonon coupling^{6,26}. The importance of oxygen holes has previously been demonstrated in the Zhang-Rice model²⁷ for cuprates, in which Cu d electrons and oxygen holes form a strongly hybridized singlet state, highlighting their potential role in understanding the CDW order and high- T_c superconductivity in the bismuthates as well.

In spite of their scientific importance, a contrastive analysis of the effects of bismuth and oxygen has so far been limited due to lack of compounds analogous to the bismuthates. Perovskite antimonates are ideal candidates to study, because antimony is isovalent to bismuth. In addition, higher on-site energy of the Sb 5s orbital compared to the Bi 6s may enable us to tune Δ_{CT} of the material from negative to positive, therefore orbital characters of the states around the Fermi level are expected to be modified. Several attempts have been made to synthesize

superconducting antimonates, but with limited success. Cava *et al.* reported that partially doped $\text{BaPb}_{0.75}\text{Sb}_{0.25}\text{O}_3$ becomes superconducting²⁸, but its T_c is significantly decreased as compared to $\text{BaPb}_{0.75}\text{Bi}_{0.25}\text{O}_3$. The role of antimony has also been investigated via first-principles calculation, revealing a possible strong electron-phonon coupling in antimonates²⁹. However, superconducting perovskite antimonates, with only antimony occupying the octahedral sites of perovskites, have yet to be experimentally reported. This is probably because the strongly covalent Sb-O bond is known to hamper forming 180 degree Sb-O-Sb bonds³⁰, and as a consequence, no perovskite antimonates have been realized up to date except a highly distorted insulating NaSbO_3 ³¹. Here, we report new superconducting antimonates $\text{Ba}_{1-x}\text{K}_x\text{SbO}_3$ (BKSO), which we were able to stabilize for the first time via high-pressure high-temperature synthesis routes, enabling clarification of possible driving mechanisms for CDW and superconductivity in the compounds by comparing their properties with the sibling compound, BKBO.

In order to shed light on the effects that varying Δ_{CT} has on the electronic structure, the band structures of BKSO as well as BKBO are calculated via the hybrid-DFT method¹⁴, as shown in Fig. 1. Here we used their atomic structures without the breathing distortions, which were experimentally obtained at the potassium concentration x of ~ 0.65 as discussed later. BKBO is anticipated to have negative Δ_{CT} ^{5,6}, as explained earlier. Therefore, it should show predominant oxygen 2p character in the $sp\sigma^*$ antibonding band, and Bi 6s character in the $sp\sigma$ bonding band. The distinct characters of the two bands are clearly confirmed in the band structure calculation (For more quantitative analysis, see Extended Data Fig. 1). In contrast, we find that BKSO shows stronger Sb 5s character in the $sp\sigma^*$ band as compared to BKBO. This suggests Δ_{CT} of BKSO may be marginally positive, which is further supported by Wannierization analysis (Extended Data Fig. 2 and Table 1). In addition, both Sb 5s and oxygen 2p characters are rather

mixed in the bonding and antibonding bands (also see Extended Data Fig. 1), corroborating stronger metal-oxygen covalency in BKSO.

Having clarified the inverted Δ_{CT} of BKSO as compared to that of BKBO, we next reveal how the inversion modifies physical properties of the materials. First, the parent compound $\text{BaSbO}_{3-\delta}$ (BSO) is found to be a robust insulator with a larger CDW gap. Rietveld refinement of neutron powder diffraction data (Extended Data Fig. 3a) confirms cubic symmetry (space group $Fm\bar{3}m$) with the breathing distortion, and furthermore, reveals two distinct Sb-O bond lengths, 2.24(1) and 2.01(1) Å (Fig. 2). Surprisingly, its bond-length difference ($\Delta d = 0.23$ Å) is larger than that of BBO ($\Delta d = 2.28 - 2.11 = 0.16$ Å)⁸. The observation of the breathing distortion establishes the commensurate CDW order from the structural point of view, which results in a band gap in the material. Using diffusive reflectance spectroscopy, the band gap in BSO is determined to be 2.54 eV. The value is significantly larger than that in BBO (2.02 eV)³², consistent with the larger bond-length disproportionation observed in the neutron diffraction.

The CDW order of the antimonate can be manageably suppressed by substituting Ba with potassium up to 65 %. X-ray and neutron powder diffraction measurements enable us to map out the structural phase diagram of BKSO, as shown in Fig. 3 (For detailed refinement profiles, see Extended Data Figs. 3 and 4). As x increases, two structural transitions are found, namely, from $Fm\bar{3}m$ to $I4/mcm$ at $x \approx 0.3$, and from $I4/mcm$ to a $Pm\bar{3}m$ phase at $x \approx 0.65$. Apparently, this structural phase diagram is qualitatively similar to that of BKBO³³, in which the CDW order is sequentially suppressed from the long-range to short-range and then finally disappears. The structural transitions also trigger a drastic change in Raman scattering, as shown in Fig. 3b. The undoped compound shows a pronounced peak at 672 cm^{-1} , which corresponds to the breathing-

mode phonon, that is, the symmetric movement of oxygen ions with A_{1g} symmetry and also known to be crucial in superconductivity in BKBO³⁴. The phonon peak is first marginally softened as x increases, and next its amplitude completely vanishes for $x \geq 0.65$. Because all the phonon modes become Raman-inactive in the $Pm\bar{3}m$ phase³⁵, the vanishing breathing-mode peak confirms that the crystal symmetry above $x = 0.65$ is indeed $Pm\bar{3}m$ and that the CDW order is completely suppressed. Interestingly, the critical potassium concentration x_{IMT} at which the structure symmetry becomes $Pm\bar{3}m$ is larger in BKSO ($x_{\text{IMT}} \sim 0.65$) than in BKBO ($x_{\text{IMT}} \sim 0.35$). The larger x_{IMT} is plausibly related to the bigger CDW gap, which may necessitate more holes for its suppression in the antimonates.

BKSO, with $x = 0.67$ and $Pm\bar{3}m$ symmetry, shows bulk superconductivity with a maximum T_c of 15.0 K, as depicted in Fig. 4. Specific heat of the optimally doped sample ($x = 0.67$) shows a jump at 15.0 K due to the superconducting transition, which is suppressed by applying a magnetic field of 1 T (Fig. 4a). While the jump is broadened, perhaps indicating sample inhomogeneity from the high-pressure synthesis, the electronic specific heat $\Delta C/T$ shows a change on the order of γ ($0.924 \text{ mJ}\cdot\text{mol}^{-1}\text{K}^{-2}$; Extended Data Fig. 5), indicating bulk superconductivity. Further convincing evidence of bulk superconductivity can be found in magnetic susceptibility, with a diamagnetic volume fraction near 100 % (Fig. 4b). Importantly, the T_c of BKSO is found to be lower than the maximum T_c of BKBO ($\sim 30 \text{ K}$ at $x = 0.4$), but at the same potassium concentration, the T_c is higher than that of BKBO (7.0 K at $x = 0.66$)³⁶ by more than factor of two.

Reduced oxygen hole character in the optimally doped BKSO is revealed via X-ray absorption spectroscopy (XAS), consistent with its positive Δ_{CT} . The oxygen K -edge, which probes

unoccupied oxygen $2p$ states, is measured and compared with a BKBO reference at similar potassium concentration, as shown in Fig. 4c. As reported previously, BKBO exhibits a significant pre-peak at $E = 528.5$ eV, which indicates predominant oxygen holes in the conduction band³⁷. Interestingly, we find that BKSO shows the pre-peak at the same energy but its intensity is diminished. It should be mentioned that the Sb M_5 -edge gives rise to an additional feature in the spectrum because of its similar energy to that of the oxygen K -edge³⁸, complicating further quantitative analysis at present.

A phase diagram of BKSO, compiled from these results, offers a comprehensive view of the interplay between the CDW order and superconductivity in main-group oxide superconductors (Fig. 5). First, a common tendency in the phase diagram can be found in both compounds; as the CDW insulating phase is suppressed, a half-dome of superconductivity arises with T_c maximized at the border of the insulator-to-metal transition and gradually decreasing with x increased. Nevertheless, a crucial difference between the two compounds is that the suppression of the CDW phase occurs at higher x in BKSO, possibly related with its larger CDW gap. As BKSO shows higher T_c at $x \geq 0.65$, its T_c could have exceeded that of BKBO if it were possible to stabilize metallic BKSO at lower x and the same trend of T_c on x held. In reality, this is so far prohibited by the strong CDW instability in BKSO, setting a limit on enhancing superconductivity further.

Though its T_c is lower than the maximum value of BKBO, enhanced superconductivity in BKSO at $x = 0.65$ suggests a mechanism associated with strong metal-oxygen covalency. Strong covalency in BKSO can be basically understood as a consequence of decreased absolute value of Δ_{CT} , making the orbital energies of Sb $5s$ and O $2p$ very close (Fig. 1d). As a result, Sb-O bonds are expected to be stiffer than Bi-O bonds, giving rise to increased phonon energy, which is

indeed supported by experiments: First, the Debye temperature of the optimally doped BKSO is found to be 535 K (Extended Data Fig. 4), which is greater than that of BKBO, typically ~ 330 K³⁹. Second, the breathing-mode phonon in the parent compounds show its frequency increased by about 19 % in BSO (672 cm^{-1}), as compared to BBO³⁵ (565 cm^{-1} ; Extended Data Fig. 6). Taking a simple approach assuming that superconductivity in BKSO arises from electrons strongly coupled to the high-energy breathing phonon, our results indicate that electron-phonon coupling may be stronger in BKSO than in BKBO (see Method section for more detailed discussion). Larger CDW instability in BKSO could also be related to its stronger electron-phonon coupling, which is reminiscent of covalent superconductors in which too large electron-phonon coupling sometimes leads to lattice instability instead of higher T_c ^{40,41}.

Finally, yet importantly, our study affords a new insight into the role of negative Δ_{CT} and oxygen holes. On one hand, it is evident from the results that BKSO, which has positive Δ_{CT} , demonstrates both CDW insulating and superconducting phases, analogous to BKBO. Therefore, the emergence of the two phases is not necessarily dependent on the sign of Δ_{CT} . In addition, at $x \geq 0.65$ BKSO shows even higher T_c than BKBO, in spite of its decreased oxygen hole character. Hence, it could be inferred that oxygen holes may not be a *necessary* condition for enhancement of superconductivity. On the other hand, BKBO, which has more oxygen holes, shows the unexpectedly smaller amplitude of the CDW order than that in BKSO, which results in a smaller x_{IMT} as well. Since the electronic DOS as well as electron-phonon interaction become larger with decreasing x ¹⁸, it would be naturally anticipated that a smaller x_{IMT} may lead to an increased T_c . Therefore, the weakened CDW order in BKBO, possibly by oxygen holes, could be vital to show a higher T_c . In this respect, oxygen holes may be a *sufficient* condition for a higher T_c ⁴².

In conclusion, we have reported the discovery of new superconducting perovskite antimonates with a maximum T_c of 15 K. The modification of Δ_{CT} via the substitution of Bi to Sb has allowed us to address long-standing questions as to the different roles of metal and oxygen ions for the CDW and superconductivity in the main-group oxide superconductors. Furthermore, these results provide fascinating possibilities for approaching novel regimes in the future. It would be interesting to change Δ_{CT} either to be more positive or negative by choosing appropriate elements at the octahedral site: arsenic and tin would give an on-site energy of ns level higher than antimony, thus their Δ_{CT} would be more positive than antimonates. Assuming these compounds can be stabilized, they would show more prominent effects of the cations, providing ideal model systems to examine the negative U model and the effects of valence fluctuations³. On the other hand, tellurium⁴³ and iodine⁴⁴ would give an on-site energy of ns level lower than antimony, and perhaps comparable or even lower than bismuth. Thus their Δ_{CT} would be more negative than antimonates and possibly bismuthates. Depending on their energy level relative to the Bi 6s level, they could provide additional model systems to comprehensively examine the effect of oxygen holes⁵.

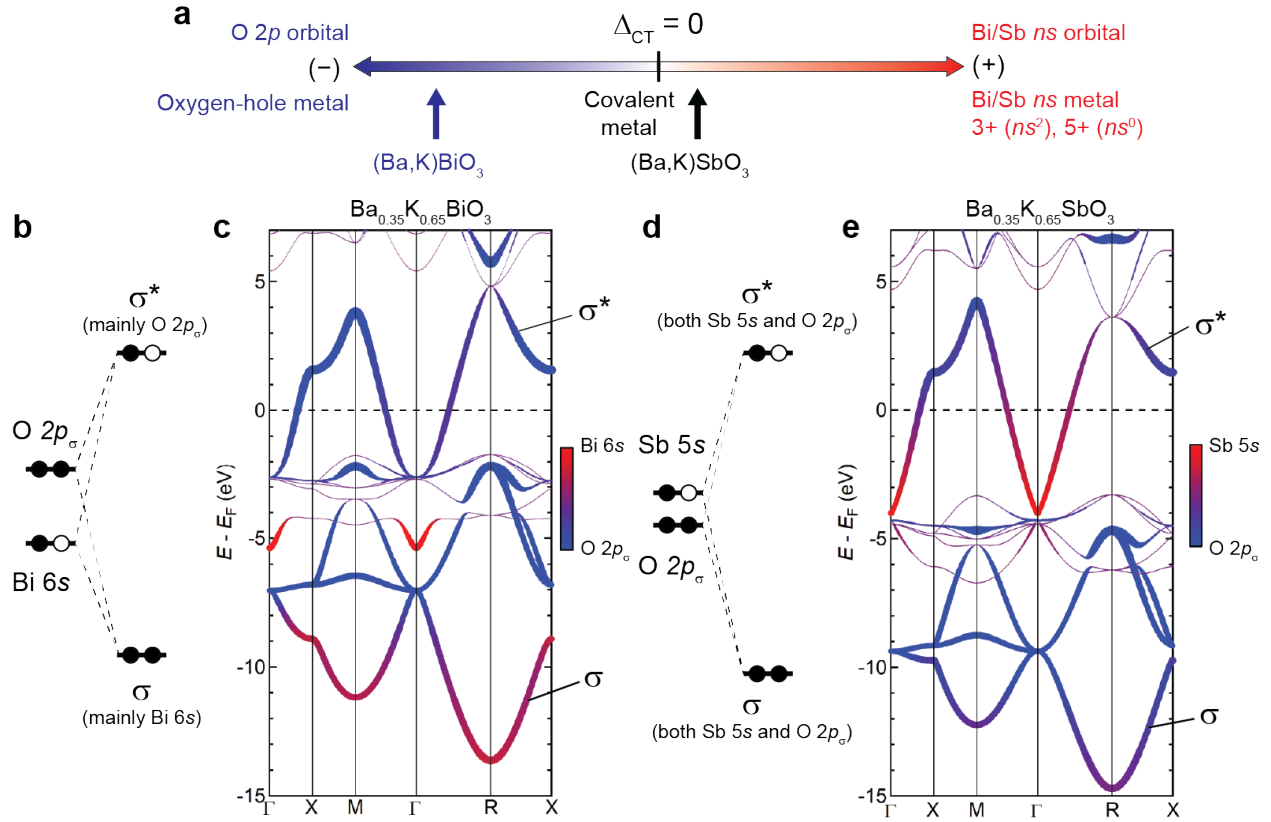


Figure 1 | Inverted charge transfer energy of the antimonate as compared to the bismuthate. **a**, A schematic diagram of different regimes of metallicity in $\text{Ba}_{1-x}\text{K}_x\text{BiO}_3$ (BKBO) and $\text{Ba}_{1-x}\text{K}_x\text{SbO}_3$ (BKSO). When charge transfer energy Δ_{CT} is positive, Bi or Sb *s* electrons are dominant. On the contrary, when it is negative, oxygen holes become dominant. BKBO is presumably located in the scheme of the oxygen-hole metal (Δ_{CT} is negative)^{5,6}, because the Bi $6s$ orbital energy is markedly lower than the O $2p$ energy, as illustrated in its molecular orbital diagram, **b**. **c**, The fat-band representation of its electronic band structure calculated with hybrid-DFT confirms the predominant oxygen (bismuth) character in the σ^* (σ) band, consistent with that expected from negative Δ_{CT} . Meanwhile, BKSO is located rather in the scheme of the Bi/Sb *s*-orbital metal, in which the charge transfer energy is slightly positive while being close to the middle ($\Delta_{\text{CT}} \gtrsim 0$). This is due to the higher Sb $5s$ orbital energy as depicted in its molecular

orbital diagram, **d**. The diagram is supported by the hybrid-DFT calculations, **e**. BKSO clearly shows a relatively stronger Sb 5s character in the σ^* band as compared to BKBO, while both Sb 5s and oxygen 2p are found to be highly mixed in both σ and σ^* bands, indicating strong Sb-O covalency.

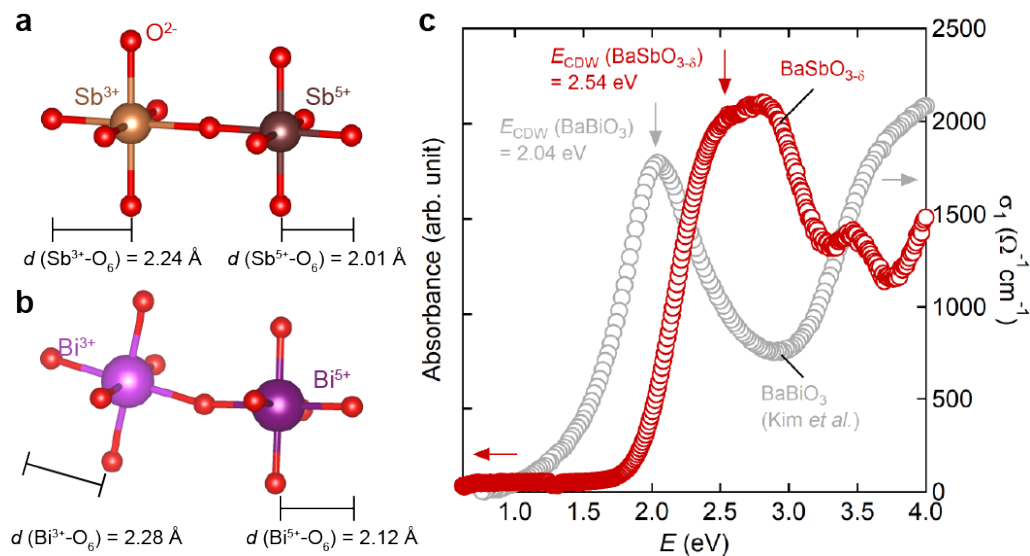


Figure 2 | Three-dimensional charge density wave order in undoped $\text{BaSbO}_{3-\delta}$. Schematic diagrams of expanded and contracted octahedra in **a**, $\text{BaSbO}_{3-\delta}$ and **b**, BaBiO_3 . From the neutron diffraction investigations, two distinct Sb-O bond lengths are estimated to be 2.24(1) and 2.01(1) Å, respectively. Its bond-length difference is found to be larger than that of BaBiO_3 ⁸. **c**, Optical absorbance of $\text{BaSbO}_{3-\delta}$ at 300 K shows a wide band gap of 2.54 eV caused by the formation of the charge-density-wave (CDW) order. For the comparison, the optical conductivity of BaBiO_3 ⁴⁵ is plotted as a reference, indicating the CDW gap of $\text{BaSbO}_{3-\delta}$ is larger than that of BaBiO_3 .

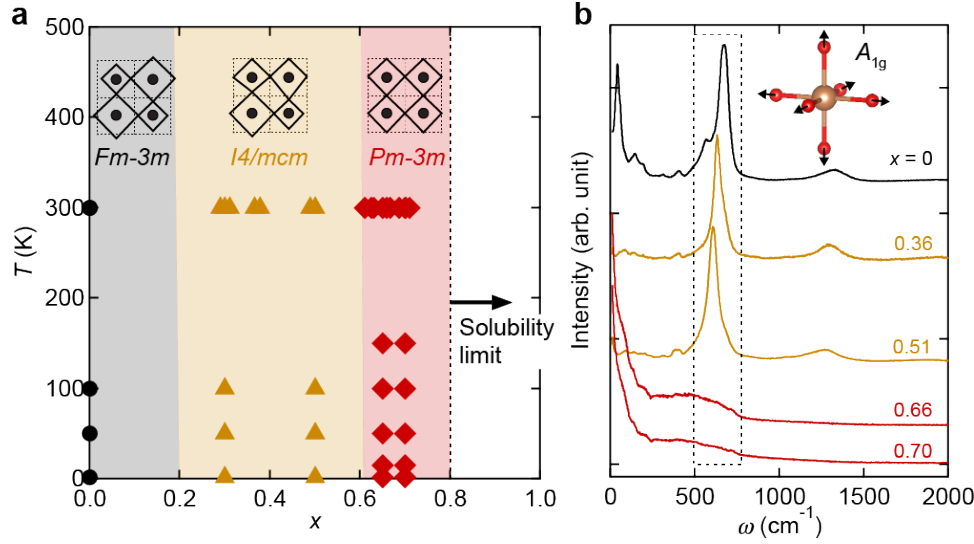


Figure 3 | Suppression of the charge density wave order via potassium doping. **a**, The structural phase diagram of $\text{Ba}_{1-x}\text{K}_x\text{SbO}_3$ based on X-ray and neutron diffraction data. Black dots, khaki triangles, and red diamonds represent the $Fm\bar{3}m$, $I4/mcm$, and $Pm\bar{3}m$ phases, respectively. The insets depict the local atomic structure of each phase, which shows transitions of the charge density wave (CDW) order from the commensurate long-range ($Fm\bar{3}m$) to short-range ($I4/mcm$), and finally to complete suppression ($Pm\bar{3}m$). **b**, Raman scattering, measured with the excitation wavelength of 632 nm at 300 K, shows that the breathing-mode phonon peak observed in $Fm\bar{3}m$ and $I4/mcm$ phases disappears in the $Pm\bar{3}m$ phase ($x \geq 0.65$), confirming the CDW order is completely suppressed. The inset shows a schematic picture of the breathing-mode phonon.

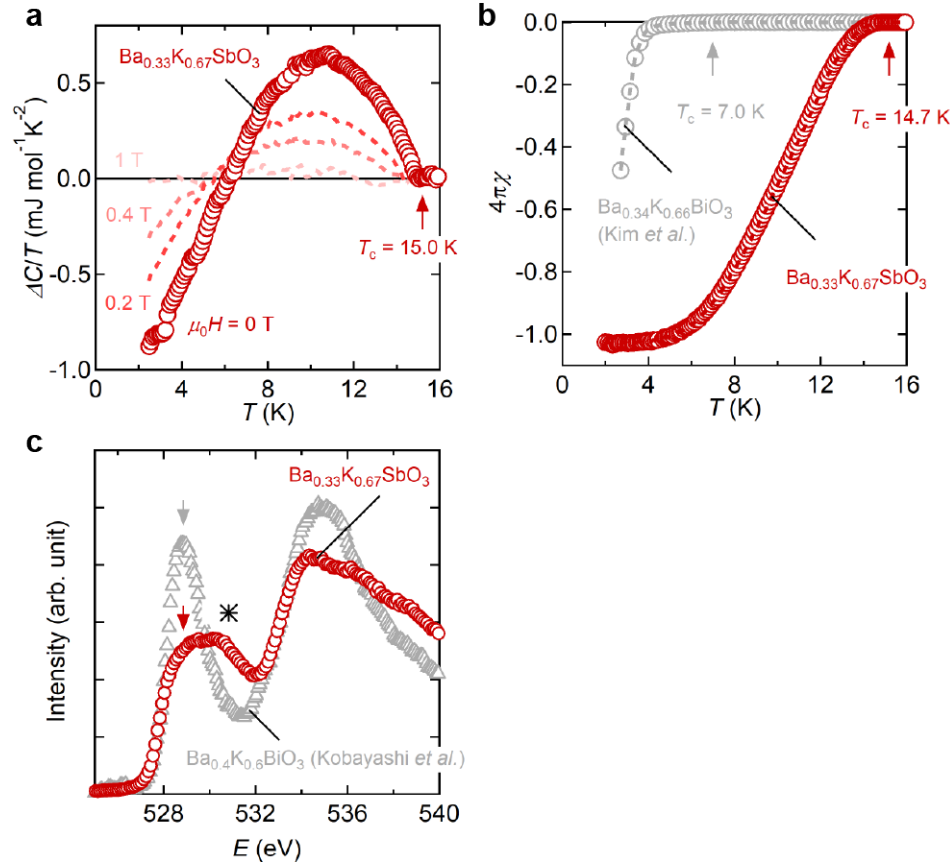


Figure 4 | Bulk superconductivity and weakened oxygen hole character in the optimally doped $\text{Ba}_{1-x}\text{K}_x\text{SbO}_3$. **a**, Superconducting transition observed in the specific heat of the optimally doped antimonate ($x = 0.67$). ΔC denotes the difference between specific heats under each field and 14 T. Superconducting transition temperature T_c is estimated to 15.0 K from the jump, which can be suppressed by applying a field of 1 T. **b**, The superconducting transition of the same sample is observed in zero-field-cooled magnetic susceptibility at 0.001 T (red), in comparison with that of $\text{Ba}_{0.34}\text{K}_{0.66}\text{BiO}_3$ (grey)³⁶. The diamagnetic volume fraction is near 100 %, indicating bulk superconductivity. Here, T_c is defined as a temperature where the volume fraction started increasing by 0.1 %. **c**, Oxygen K -edge X-ray absorption spectrum of $\text{Ba}_{0.33}\text{K}_{0.67}\text{SbO}_3$ (red open circles) at 300 K, plotted together with that of $\text{Ba}_{0.4}\text{K}_{0.6}\text{BiO}_3$ ³⁷ (grey open triangles). The intensity of each spectrum was calibrated such that the intensity at a higher energy (~ 550 eV)

above the edge between two samples is to be equal. The decreased prepeak in the antimonate, shown by arrows, indicates the decrease of oxygen holes compared to the bismuthate. The peak indicated by the asterisk may be due to the Sb M_5 -edge, whose energy is close to the oxygen K -edge.

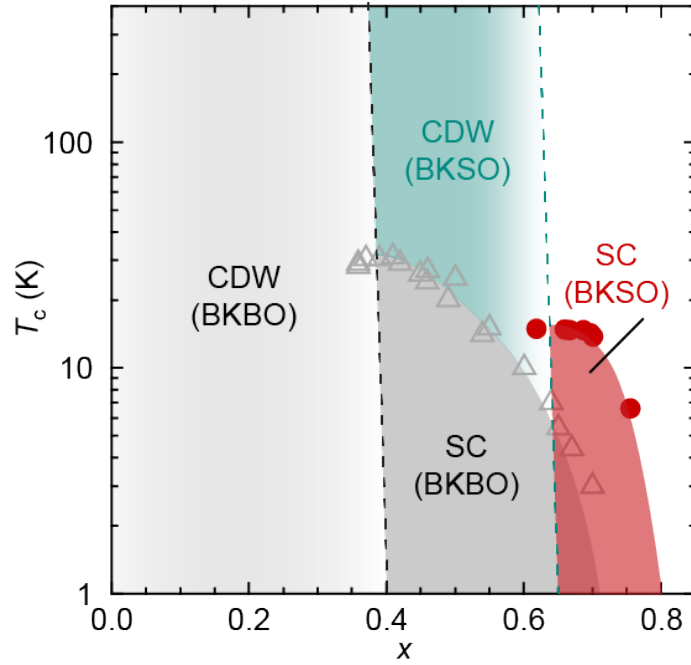


Figure 5 | Phase diagram of charge density waves (CDW) and superconductivities (SC) in $\text{Ba}_{1-x}\text{K}_x\text{SbO}_3$ (BKSO) and $\text{Ba}_{1-x}\text{K}_x\text{BiO}_3$ (BKBO). Red circles are the T_c 's of the antimonates with the same notation as in Figure 3, and grey triangles are T_c of $\text{Ba}_{1-x}\text{K}_x\text{BiO}_3$ ^{36,46}. T_c of the antimonates show a half-dome shape (red region), which is similar to that of the bismuthates (dark grey). The crucial difference is that the CDW order in the bismuthates (light grey region) is suppressed at $x = 0.4$, whereas that of the antimonates (green region) continues to exist up to $x = 0.65$.

Methods

Sample synthesis and characterization (Ba,K)SbO₃ samples were fabricated using a high-pressure high-temperature synthesis technique with a Walker-type multi-anvil module. A typical synthesis condition was ~1200 °C at 12 GPa. Powder X-ray diffraction was measured in the Debye-Scherrer geometry using a Mo $K\alpha_1$ source. Neutron powder diffraction was measured with a time-of-flight neutron source using the instrument WISH at ISIS. Optical absorbance was measured via diffuse reflectance spectroscopy at room temperature. Magnetic susceptibility and heat capacity were measured via a Quantum Design magnetic property measurement system (MPMS) and physical property measurement system (PPMS), respectively. X-ray absorption spectroscopy (XAS) is measured in partial fluorescence yield mode using a silicon drift detector to select the O K -edge fluorescence, at the Spherical Grating Monochromator (SGM) beamline at the Canadian Light Source.

First-principles calculation The band structures of BKSO and BKBO were calculated using the WIEN2k code⁴⁷ with full hybrid functionals (YS-PBE0, similar to HSE06⁴⁸). For the calculations, $10 \times 10 \times 10$ k mesh, $R_{MT}K_{MAX} = 7.0$, and the virtual crystal approximation were used. The atomic structures reported from experiments were used.

Comparison of T_c between BKSO and BKBO at $x = 0.65$ Here we assume that superconductivity in both BKSO and BKBO is primarily caused by electrons strongly coupled with the high-frequency breathing phonon. According to the McMillan-Hopfield expression^{49,50} for superconductors in strong electron-phonon coupling regime, T_c is given as $\sqrt{\lambda \langle \omega^2 \rangle} \sim \sqrt{\eta/M}$, where λ is the electron-phonon coupling constant, $\langle \omega^2 \rangle$ is the average of squared phonon frequency, M is the atomic mass, and η is the electronic spring constant. Also, λ is given as

$N(E_F)\langle I^2 \rangle / M\langle \omega^2 \rangle$, where $N(E_F)$ is the DOS at the Fermi energy, $\langle I^2 \rangle$ is the Fermi surface average of squared electron-phonon coupling interaction. For the cases of BKSO and BKBO, M would be the mass of oxygen. Total DOS is estimated via the band calculation to be nearly identical in BKSO and BKBO (Extended Data Fig. 1). Then, the above expression of T_c can be simplified to $T_c \propto \sqrt{\langle I^2 \rangle}$. Therefore, increased T_c in BKSO can be understood by increased $\langle I^2 \rangle$.

Acknowledgement We thank P. Adler, K. Foyevtsova, G. Khaliullin, H. Mizoguchi, J.-G. Park, and J. Yu for discussions, and U. Engelhardt, F. Falkenberg, W. Kain, K. Schunke, and S. Strobel for experimental support. This research was carried out owing in part to funding from the Max Planck-UBC-UTokyo Centre for Quantum Materials. The Canadian Light Source (CLS) is funded by the Canada Foundation for Innovation, NSERC, the National Research Council of Canada, the Canadian Institutes of Health Research, the Government of Saskatchewan, Western Economic Diversification Canada, and the University of Saskatchewan. We thank the STFC ISIS facility for the provision of beamtime.

Author Contributions H.T. and M.K. conceived the project. M.K. prepared and characterized the samples. T.T., M.I., and R.K.K. helped the analysis. M.K., G.M.M., A.G., and P.M. conducted the neutron diffraction experiments. M.K. and H.-H.K. conducted the Raman experiments. M.K. and U.W. and A.Y. performed the first-principles calculations. M.O. and R.G. conducted the XAS experiments. M.K. and H.T. wrote manuscript and all authors commented on it.

Competing interests The authors declare no competing interests.

Additional information

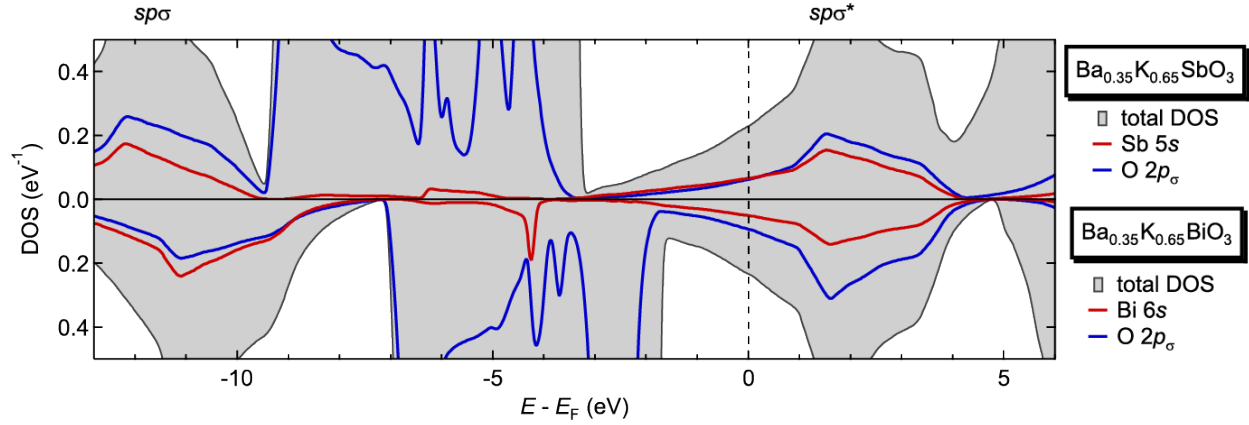
Correspondence and requests for materials Should be addressed to M.K. or H.T.

Reference

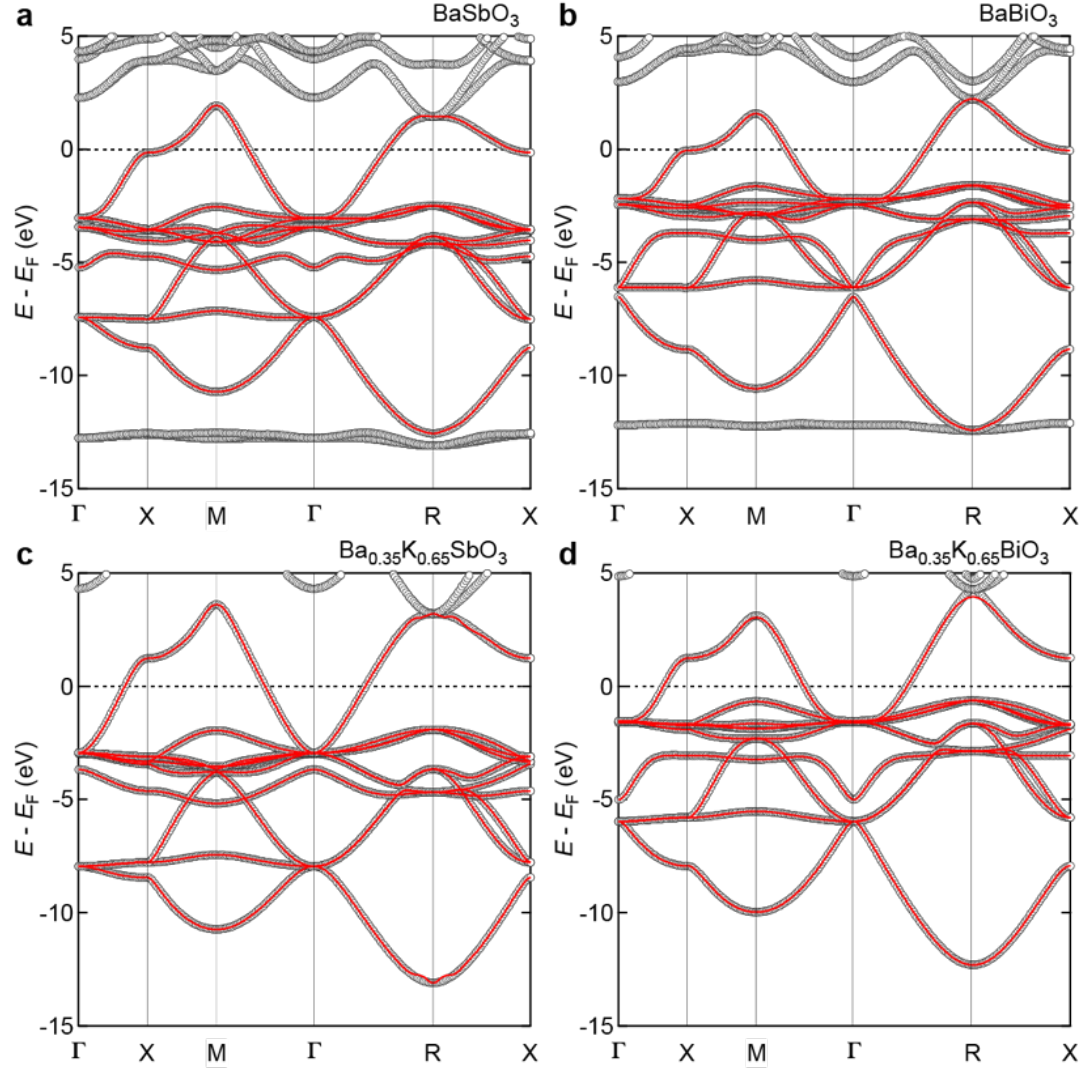
- 1 Mattheiss, L. F., Gyorgy, E. M. & Johnson, D. W. Superconductivity above 20 K in the Ba-K-Bi-O system. *Phys. Rev. B* **37**, 3745-3746, doi:10.1103/PhysRevB.37.3745 (1988).
- 2 Cava, R. J. *et al.* Superconductivity near 30 K without copper: the $\text{Ba}_{0.6}\text{K}_{0.4}\text{BiO}_3$ perovskite. *Nature* **332**, 814-816, doi:10.1038/332814a0 (1988).
- 3 Varma, C. M. Missing valence states, diamagnetic insulators, and superconductors. *Phys. Rev. Lett.* **61**, 2713-2716, doi:10.1103/PhysRevLett.61.2713 (1988).
- 4 Rice, T. M. & Sneddon, L. Real-space and k-space electron pairing in $\text{BaPb}_{1-x}\text{Bi}_x\text{O}_3$. *Phys. Rev. Lett.* **47**, 689-692, doi:10.1103/PhysRevLett.47.689 (1981).
- 5 Foyevtsova, K., Khazraie, A., Elfimov, I. & Sawatzky, G. A. Hybridization effects and bond disproportionation in the bismuth perovskites. *Phys. Rev. B* **91**, 121114, doi:10.1103/PhysRevB.91.121114 (2015).
- 6 Khazraie, A., Foyevtsova, K., Elfimov, I. & Sawatzky, G. A. Oxygen holes and hybridization in the bismuthates. *Phys. Rev. B* **97**, 075103, doi:10.1103/PhysRevB.97.075103 (2018).
- 7 Sleight, A. W., Gillson, J. L. & Bierstedt, P. E. High-temperature superconductivity in $\text{BaPb}_{1-x}\text{Bi}_x\text{O}_3$ system. *Solid State Commun.* **17**, 27-28, doi:10.1016/0038-1098(75)90327-0 (1975).
- 8 Cox, D. E. & Sleight, A. W. Crystal structure of $\text{Ba}_2\text{Bi}^{3+}\text{Bi}^{5+}\text{O}_6$. *Solid State Commun.* **19**, 969-973, doi:10.1016/0038-1098(76)90632-3 (1976).
- 9 Thonhauser, T. & Rabe, K. M. Fcc breathing instability in BaBiO_3 from first principles. *Phys. Rev. B* **73**, 212106, doi:10.1103/PhysRevB.73.212106 (2006).
- 10 Mattheiss, L. F. & Hamann, D. R. Electronic structure of $\text{BaPb}_{1-x}\text{Bi}_x\text{O}_3$. *Phys. Rev. B* **28**, 4227-4241, doi:10.1103/PhysRevB.28.4227 (1983).
- 11 Mattheiss, L. F. & Hamann, D. R. Electronic structure of the high- T_c superconductor $\text{Ba}_{1-x}\text{K}_x\text{BiO}_3$. *Phys. Rev. Lett.* **60**, 2681-2684, doi:10.1103/PhysRevLett.60.2681 (1988).
- 12 Huang, Q. *et al.* Tunneling evidence for predominantly electron phonon coupling in superconducting $\text{Ba}_{1-x}\text{K}_x\text{BiO}_3$ and $\text{Nd}_{2-x}\text{Ce}_x\text{CuO}_{4-y}$. *Nature* **347**, 369-372, doi:10.1038/347369a0 (1990).
- 13 Hinks, D. G., Richards, D. R., Dabrowski, B., Marx, D. T. & Mitchell, A. W. The oxygen isotope effect in $\text{Ba}_{0.625}\text{K}_{0.375}\text{BiO}_3$. *Nature* **335**, 419-421, doi:10.1038/335419a0 (1988).
- 14 Franchini, C., Kresse, G. & Podloucky, R. Polaronic hole trapping in doped BaBiO_3 . *Phys. Rev. Lett.* **102**, 256402, doi:10.1103/PhysRevLett.102.256402 (2009).
- 15 Nourafkan, R., Marsiglio, F. & Kotliar, G. Model of the electron-phonon interaction and optical conductivity of $\text{Ba}_{1-x}\text{K}_x\text{BiO}_3$ superconductors. *Phys. Rev. Lett.* **109**, 017001, doi:10.1103/PhysRevLett.109.017001 (2012).
- 16 Yin, Z. P., Kutepov, A. & Kotliar, G. Correlation-enhanced electron-phonon coupling: applications of GW and screened hybrid functional to bismuthates, chloronitrides, and other high- T_c superconductors. *Phys. Rev. X* **3**, 021011, doi:10.1103/PhysRevX.3.021011 (2013).
- 17 Wen, C. H. P. *et al.* Unveiling the superconducting mechanism of $\text{Ba}_{0.51}\text{K}_{0.49}\text{BiO}_3$. *Phys. Rev. Lett.* **121**, 117002, doi:10.1103/PhysRevLett.121.117002 (2018).
- 18 Li, Z. L., Antonius, G., Wu, M., da Jornada, F. H. & Louie, S. G. Electron-phonon coupling from ab initio linear-response theory within the GW method: correlation-enhanced interactions and superconductivity in $\text{Ba}_{1-x}\text{K}_x\text{BiO}_3$. *Phys. Rev. Lett.* **122**, 186402, doi:10.1103/PhysRevLett.122.186402 (2019).
- 19 Anderson, P. W. Model for the electronic structure of amorphous semiconductors. *Phys. Rev. Lett.* **34**, 953-955, doi:10.1103/PhysRevLett.34.953 (1975).
- 20 Emery, V. J. Theory of the quasi-one-dimensional electron gas with strong "on-site" interactions. *Phys. Rev. B* **14**, 2989-2994, doi:10.1103/PhysRevB.14.2989 (1976).

- 21 Matsushita, Y., Bluhm, H., Geballe, T. H. & Fisher, I. R. Evidence for charge Kondo effect in superconducting Tl-doped PbTe. *Phys. Rev. Lett.* **94**, 157002, doi:10.1103/PhysRevLett.94.157002 (2005).
- 22 Ignatov, A. Y. Relationship between the electronic and local structure in $\text{BaPb}_x\text{Bi}_{1-x}\text{O}_3$ and $\text{Ba}_{1-x}\text{K}_x\text{BiO}_3$ perovskites. *Nucl. Instrum. Methods Phys. Res. A* **448**, 332-339, doi:10.1016/s0168-9002(99)00691-9 (2000).
- 23 Pyykko, P. Relativistic effects in structural chemistry. *Chem. Rev.* **88**, 563-594, doi:10.1021/cr00085a006 (1988).
- 24 Wertheim, G. K., Remeika, J. P. & Buchanan, D. N. E. Electronic structure of $\text{BaPb}_{1-x}\text{Bi}_x\text{O}_3$. *Phys. Rev. B* **26**, 2120-2123, doi:10.1103/PhysRevB.26.2120 (1982).
- 25 Shen, Z. X. *et al.* Photoemission study of monoclinic BaBiO_3 . *Phys. Rev. B* **40**, 6912-6918, doi:10.1103/PhysRevB.40.6912 (1989).
- 26 Hirsch, J. E. & Marsiglio, F. Superconducting state in an oxygen hole metal. *Phys. Rev. B* **39**, 11515-11525, doi:10.1103/PhysRevB.39.11515 (1989).
- 27 Zhang, F. C. & Rice, T. M. Effective hamiltonian for the superconducting Cu oxides. *Phys. Rev. B* **37**, 3759-3761, doi:10.1103/PhysRevB.37.3759 (1988).
- 28 Cava, R. J. *et al.* Superconductivity at 3.5 K in $\text{BaPb}_{0.75}\text{Sb}_{0.25}\text{O}_3$ - Why is T_c so low. *Nature* **339**, 291-293, doi:10.1038/339291a0 (1989).
- 29 Julien, J. P., Papaconstantopoulos, D. A., Cyrotlackmann, F. & Pasturel, A. Calculations of the electronic structure and superconducting properties of $\text{BaPb}_{1-x}\text{Sb}_x\text{O}_3$. *Phys. Rev. B* **43**, 2903-2909, doi:10.1103/PhysRevB.43.2903 (1991).
- 30 Goodenough, J. B. & Kafalas, J. A. Exploring $\text{A}^+\text{B}^{5+}\text{O}^3$ compounds. *J. Solid State Chem.* **6**, 493-501, doi:10.1016/s0022-4596(73)80005-2 (1973).
- 31 Mizoguchi, H., Woodward, P. M., Byeon, S. H. & Parise, J. B. Polymorphism in NaSbO_3 : structure and bonding in metal oxides. *J. Am. Chem. Soc.* **126**, 3175-3184, doi:10.1021/ja038365h (2004).
- 32 Sato, H., Tajima, S., Takagi, H. & Uchida, S. Optical study of the metal-insulator transition on $\text{Ba}_{1-x}\text{K}_x\text{BiO}_3$ thin-films. *Nature* **338**, 241-243, doi:10.1038/338241a0 (1989).
- 33 Pei, S. Y. *et al.* Structural phase diagram of the $\text{Ba}_{1-x}\text{K}_x\text{BiO}_3$ system. *Phys. Rev. B* **41**, 4126-4141, doi:10.1103/PhysRevB.41.4126 (1990).
- 34 Loong, C. K. *et al.* High-energy oxygen phonon modes and superconductivity in $\text{Ba}_{1-x}\text{K}_x\text{BiO}_3$ - an inelastic-neutron-scattering experiment and molecular-dynamics simulation. *Phys. Rev. Lett.* **62**, 2628-2631, doi:10.1103/PhysRevLett.62.2628 (1989).
- 35 Tajima, S., Yoshida, M., Koshizuka, N., Sato, H. & Uchida, S. Raman-scattering study of the metal-insulator transition in $\text{Ba}_{1-x}\text{K}_x\text{BiO}_3$. *Phys. Rev. B* **46**, 1232-1235, doi:10.1103/PhysRevB.46.1232 (1992).
- 36 Kim, D. C. *et al.* High pressure synthesis and superconductivity of $\text{Ba}_{1-x}\text{K}_x\text{BiO}_3$ ($0.35 < x < 1$). *Physica C* **383**, 343-353, doi:10.1016/s0921-4534(02)01332-1 (2003).
- 37 Kobayashi, K. *et al.* Doping dependence of the electronic structure of $\text{Ba}_{1-x}\text{K}_x\text{BiO}_3$ studied by X-ray-absorption spectroscopy. *Phys. Rev. B* **59**, 15100-15106, doi:10.1103/PhysRevB.59.15100 (1999).
- 38 Garbassi, F. XPS and AES study of antimony oxides. *Surf. Interface Anal.* **2**, 165-169, doi:10.1002/sia.740020502 (1980).
- 39 Woodfield, B. F., Wright, D. A., Fisher, R. A., Phillips, N. E. & Tang, H. Y. Superconducting-normal phase transition in $(\text{Ba}_{1-x}\text{K}_x)\text{BiO}_3$, $x = 0.40, 0.47$. *Phys. Rev. Lett.* **83**, 4622-4625, doi:10.1103/PhysRevLett.83.4622 (1999).
- 40 Moussa, J. E. & Cohen, M. L. Two bounds on the maximum phonon-mediated superconducting transition temperature. *Phys. Rev. B* **74**, 094520, doi:10.1103/PhysRevB.74.094520 (2006).
- 41 Esterlis, I., Kivelson, S. A. & Scalapino, D. J. A bound on the superconducting transition temperature. *npj Quantum Mater.* **3**, 59, doi:10.1038/s41535-018-0133-0 (2018).

- 42 Benam, M. R., Foyevtsova, K., Khazraie, A., Elfimov, I. & Sawatzky, G. A. Holes' character and
bond versus charge disproportionation in s - p ABX_3 perovskites. arXiv:2104.07771 (2021).
- 43 Christy, A. G., Mills, S. J. & Kampf, A. R. A review of the structural architecture of tellurium
oxycompounds. *Mineral. Mag.* **80**, 415-545, doi:10.1180/minmag.2016.080.093 (2016).
- 44 Volonakis, G., Sakai, N., Snaith, H. J. & Giustino, F. Oxide analogs of halide perovskites and the
new semiconductor Ba_2AgIO_6 . *J. Phys. Chem. Lett.* **10**, 1722-1728,
doi:10.1021/acs.jpclett.9b00193 (2019).
- 45 Kim, G. *et al.* Suppression of three-dimensional charge density wave ordering via thickness
control. *Phys. Rev. Lett.* **115**, 226402, doi:10.1103/PhysRevLett.115.226402 (2015).
- 46 Nagata, Y., Mishiro, A., Uchida, T., Ohtsuka, M. & Samata, H. Normal-state transport properties
of $Ba_{1-x}K_xBiO_3$ crystals. *J. Phys. Chem. Solids* **60**, 1933-1942, doi:10.1016/s0022-
3697(99)00217-6 (1999).
- 47 Blaha, P. *et al.* WIEN2k: An APW+lo program for calculating the properties of solids. *J. Chem.*
Phys. **152**, 074101, doi:10.1063/1.5143061 (2020).
- 48 Krukau, A. V., Vydrov, O. A., Izmaylov, A. F. & Scuseria, G. E. Influence of the exchange
screening parameter on the performance of screened hybrid functionals. *J. Chem. Phys.* **125**,
224106, doi:10.1063/1.2404663 (2006).
- 49 Allen, P. B. & Dynes, R. C. Transition temperature of strong-coupled superconductors reanalyzed.
Phys. Rev. B **12**, 905-922, doi:10.1103/PhysRevB.12.905 (1975).
- 50 Hopfield, J. J. Angular momentum and transition-metal superconductivity. *Phys. Rev.* **186**, 443-
451, doi:10.1103/PhysRev.186.443 (1969).



Extended Data Figure 1 | Electronic density of states of BKSO and BKBO calculated via the hybrid-DFT method. While total DOS at Fermi level shows almost no difference between the two compounds (BKSO: 0.229 states/eV, BKBO: 0.230 states/eV), projected DOS (PDOS) of metal s and oxygen $2p_\sigma$ show meaningful differences: in BKBO, PDOS of O $2p_\sigma$ is bigger than Bi $6s$ [PDOS (Bi $6s$) / PDOS (O $2p_\sigma$) \cong 0.548]. On the contrary, in BKSO, PDOS of Sb $5s$ and O $2p_\sigma$ at the Fermi level are almost equal in BKSO [PDOS(Sb $5s$) / PDOS (O $2p_\sigma$) \cong 1.06]. The results are consistent with those suggested from the molecular-orbital diagram (Fig. 1); BKBO with negative Δ_{CT} shows predominant Bi $6s$ and O $2p_\sigma$ characters in the $sp\sigma$ bonding and $sp\sigma^*$ antibonding bands, respectively. On the contrary, BKSO, with Δ_{CT} slightly positive while close to zero, shows that the ratio between Sb $5s$ and O $2p_\sigma$ PDOS is largely unchanged in the bonding and antibonding bands. In addition, PDOS of the two orbitals at the Fermi level are almost equal.

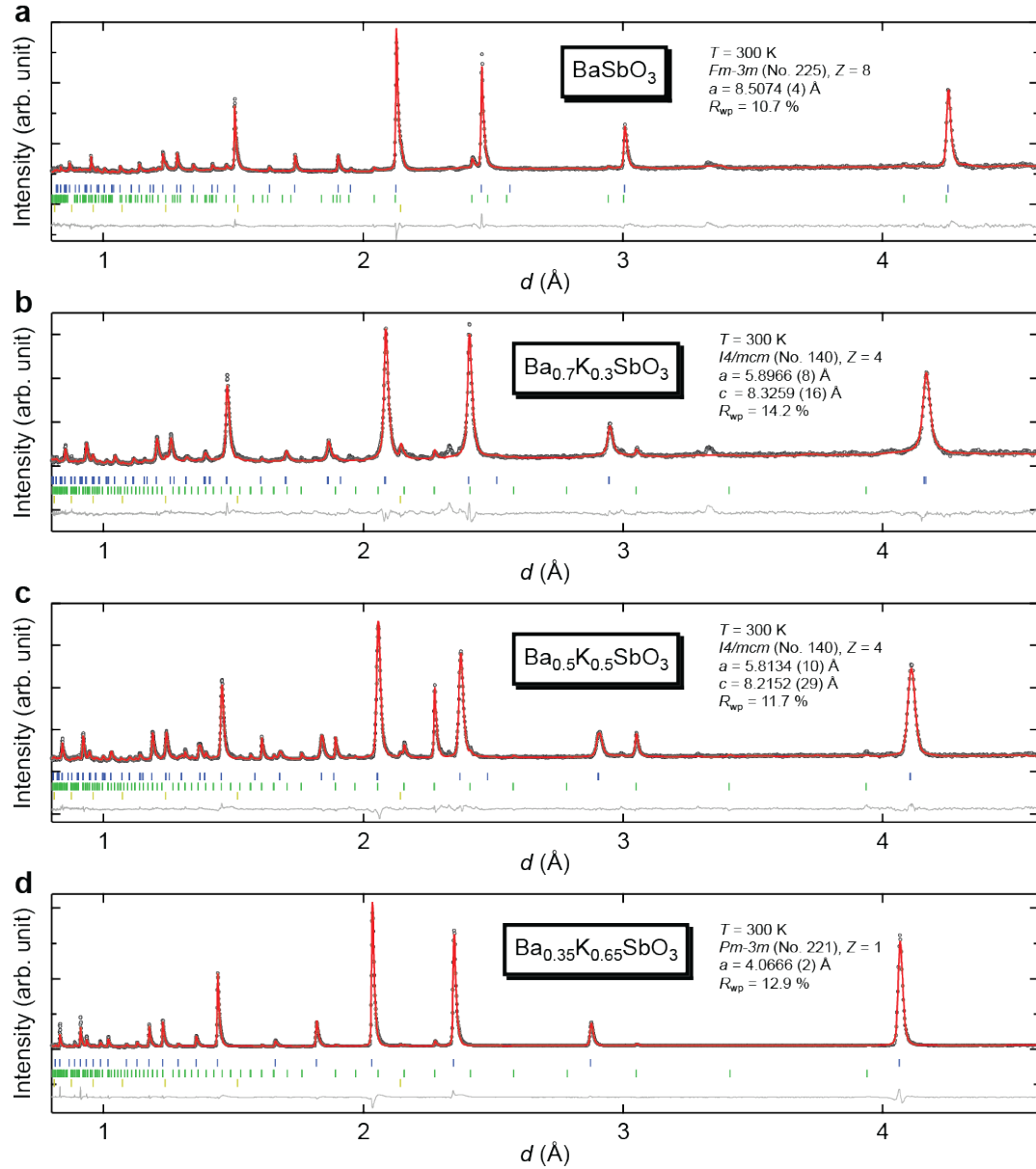


Extended Data Figure 2 | Wannierization of BKSO and BKBO without and with potassium doping. For Wannierization, density functional calculation on the band structures of **a**, BaSbO₃, **b**, BaBiO₃, **c**, Ba_{0.35}K_{0.65}SbO₃, **d**, Ba_{0.35}K_{0.65}BiO₃ were performed with the WIEN2k code using the PBE GGA (generalized gradient approximation) exchange correlation (black open circles). Other conditions are same as described in Methods. Wannierization using $7 \times 7 \times 7$ k mesh and 10 Wannier projections ($1 \times M$ ns + $3 \times$ oxygen $2p_x, 2p_y, 2p_z$) was performed to fit the DFT results (red curves).

Compound	E_s (eV)	$E_{p\sigma}$ (eV)	$E_{p\pi}$ (eV)	$t_{sp\sigma}$ (eV)	$\Delta_{CT} = E_s - (E_{p\sigma} + 2E_{p\pi})/3$ (eV)
BaSbO ₃	-4.029	-5.670	-3.849	1.964	0.427
BaBiO ₃	-5.298	-4.612	-2.796	1.995	-1.897
Ba _{0.35} K _{0.65} SbO ₃	-2.586	-6.045	-3.577	2.127	1.814
Ba _{0.35} K _{0.65} BiO ₃	-3.634	-4.213	-2.017	2.150	-0.885

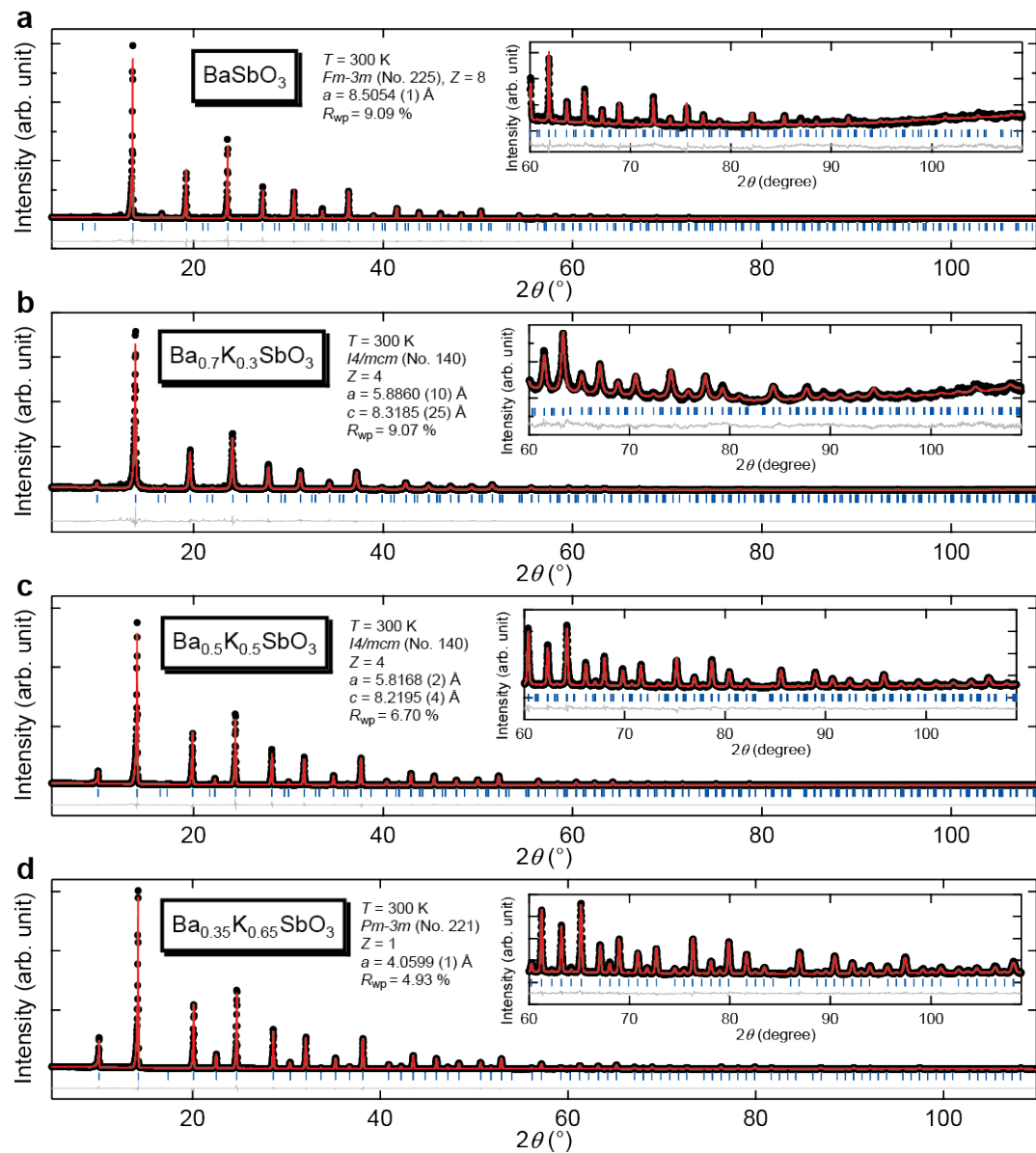
Extended Data Table 1 | Obtained parameters of BKSO and BKBO from Wannierization.

E_s , $E_{p\sigma}$, $E_{p\pi}$ are the onsite energies of M ns , O $2p_\sigma$, and O $2p_\pi$ orbitals, respectively. $t_{sp\sigma}$ is the hopping parameter between M ns and O $2p_\sigma$, and Δ_{CT} is charge transfer energy defined as energy difference between the M ns orbital and the average of O $2p_\sigma$ and O $2p_\pi$. BSO and BKSO show positive Δ_{CT} , whereas BBO and BKBO show negative Δ_{CT} . Increased Δ_{CT} in the doped compounds as compared to the undoped ones could be related to the effect of larger hybridization, as indicated by larger $t_{sp\sigma}$ in the doped compounds.

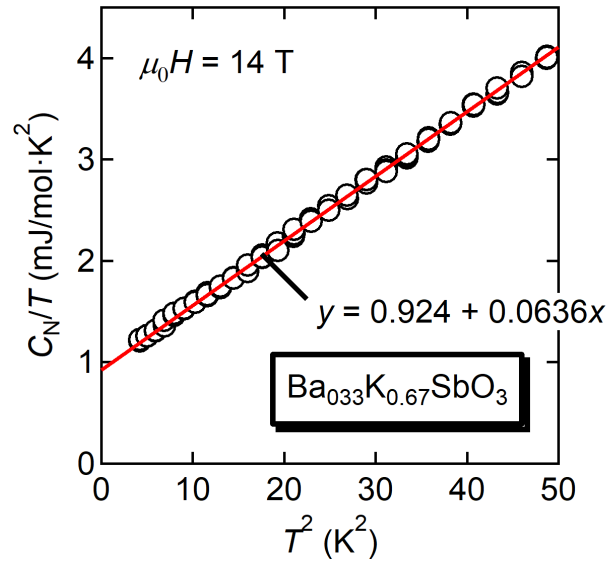


Extended Data Figure 3 | Rietveld refinement profiles of diffraction patterns of BKSO samples based on powder neutron diffraction. Neutron diffraction patterns of **a**, $\text{BaSbO}_{3-\delta}$, **b**, $\text{Ba}_{0.7}\text{K}_{0.3}\text{SbO}_3$, **c**, $\text{Ba}_{0.5}\text{K}_{0.5}\text{SbO}_3$, **d**, $\text{Ba}_{0.35}\text{K}_{0.65}\text{SbO}_3$ were collected at the WISH diffractometer, ISIS facility. Black dots are experimental data, red lines are the simulated intensity, and blue, green, and yellow ticks are the hkl indices of $\text{BaSbO}_{3-\delta}$, impurity phases ($\text{BaSbO}_{2.5}$ in $\text{BaSbO}_{3-\delta}$,

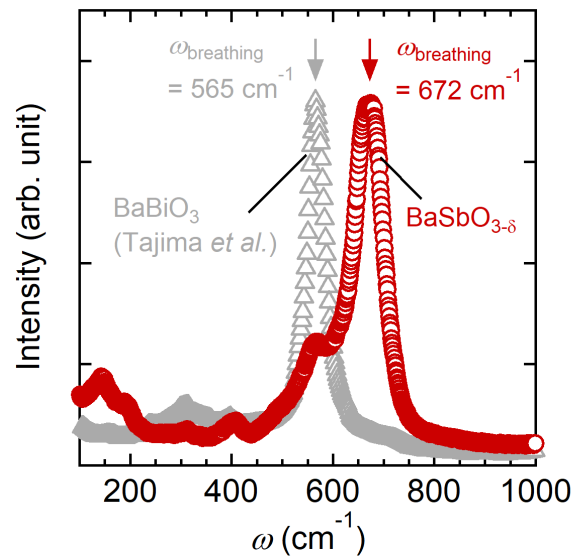
and KSbO_3 in the other three samples) and a vanadium sample can, respectively. Grey lines are the difference between the experimental data and the simulation.



Extended Data Figure 4 | Rietveld refinement profiles of diffraction patterns of BKSO samples based on powder X-ray diffraction. X-ray diffraction patterns of **a**, $\text{BaSbO}_{3-\delta}$, **b**, $\text{Ba}_{0.7}\text{K}_{0.3}\text{SbO}_3$, **c**, $\text{Ba}_{0.5}\text{K}_{0.5}\text{SbO}_3$, **d**, $\text{Ba}_{0.35}\text{K}_{0.65}\text{SbO}_3$ were collected in the Debye-Scherrer geometry with a $\text{Mo K}\alpha_1$ radiation at room temperature. Same notations as in Extended Data Figure 2 were used for plotting data.



Extended Data Figure 5 | Normal-state specific heat of the optimally doped BKSO. Normal-state specific heat C_N of $\text{Ba}_{0.33}\text{K}_{0.67}\text{SbO}_3$ was measured at the magnetic fields of 14 T, which is far larger than the upper critical field (~ 1 T) of the compound. A fit to the data with $C_N(T) = \gamma T + \beta T^3$ yields $\gamma = 0.924 \text{ mJ}\cdot\text{mol}^{-1}\text{K}^{-2}$ and $\beta = 0.0636 \text{ mJ}\cdot\text{mol}^{-1}\text{K}^{-4}$. From the value of β , the Debye temperature of 535 K was estimated.



Extended Data Figure 6 | Increased frequency of the breathing-mode phonon in the undoped antimonate as compared to the bismuthate. The breathing-mode phonon of BaSbO_{3-δ} (red open circles) measured via Raman scattering shows 19 % increase of its frequency than that of BaBiO₃³⁵ (grey open triangles), due to the strong metal-oxygen covalency of the antimonates.